

Can a Deep Progressive Learning Method Help to Achieve High Image Quality as Total-body PET Imaging?

Taisong Wang

Department of Nuclear Medicine, Shanghai No 1 Renmin Hospital: Shanghai General Hospital

Wenli Qiao

Department of Nuclear Medicine, Shanghai General Hospital, Shanghai Jiaotong University

Ying Wang

United Imaging Healthcare

Jingyi Wang

United Imaging Healthcare

Yang Lv

United Imaging Healthcare

Yun Dong

United Imaging Healthcare

Zheng Qian

United Imaging Healthcare

Yan Xing

Department of Nuclear Medicine, Shanghai General Hospital, Shanghai Jiaotong University

Jinhua Zhao (✉ zhaojinhua1963@126.com)

Department of Nuclear Medicine, Shanghai General Hospital, Shanghai Jiaotong University School of Medicine <https://orcid.org/0000-0002-8867-7985>

Research Article

Keywords: PET, deep progressive learning, low dose, image quality

Posted Date: December 15th, 2021

DOI: <https://doi.org/10.21203/rs.3.rs-1150113/v1>

License:   This work is licensed under a Creative Commons Attribution 4.0 International License.

[Read Full License](#)

1 Can a deep progressive learning method help to achieve high image 2 quality as total-body PET imaging?

3 Taisong Wang¹, Wenli Qiao¹, Ying Wang², Jingyi Wang², Yang Lv², Yun Dong², Zheng Qian², Yan
4 Xing¹, Jinhua Zhao¹

5
6
7 ¹*Department of Nuclear Medicine, Shanghai General Hospital, Shanghai Jiaotong University,*
8 *Shanghai, People's Republic of China,*

9 ²*United Imaging Healthcare, Shanghai, People's Republic of China,*

10
11 Taisong Wang and Wenli Qiao contributed equally to this work

12
13 Corresponding author: Yan Xing, Department of Nuclear Medicine, Shanghai General Hospital,
14 Shanghai Jiaotong University, No. 100 Haining Road, Shanghai, 200080, People's Republic of
15 China. E-mail: xy.1@163.com; and Jinhua Zhao, Department of Nuclear Medicine, Shanghai
16 General Hospital, Shanghai Jiaotong University, No. 100 Haining Road, Shanghai, 200080,
17 People's Republic of China. E-mail: zhaojinhua1963@126.com

19 Abstract

20 **Purpose** To propose and validate a total-body PET (TB-PET) guided deep progressive learning
21 method (DPR) for low-dose clinical imaging of standard axial field-of-view PET/CT scanner
22 (SAFOV-PET).

23 **Methods** List-mode raw data from a total of 182 scans were collected, including 100 patient scans
24 from a TB-PET, and 15 phantom and 67 patient scans from a SAFOV-PET. Neural networks
25 employed in DPR were trained with the high-quality images obtained from the TB-PET using a
26 progressive learning strategy and evaluated on a SAFOV-PET through three stages of studies. The
27 CTN phantom was firstly used to verify the effectiveness of protocols in DPR and OSEM
28 algorithms. Subsequently, list-mode rawdata from retrospective and prospective PET oncological
29 patients (n=26 and 41, respectively) were rebinned into short duration scans (referred as to
30 DPR_full, DPR_1/2, DPR_1/3, and DPR_1/4), and reconstructed with DPR. Full-duration data
31 were reconstructed with OSEM to generate images as a reference. In the retrospective study, the
32 image quality was evaluated using the metrics of standard uptake value (SUV) and target-to-liver
33 ratio (TLR) in lesions, and coefficient of variation (COV) in the liver, which provided evidence
34 for the subsequent study with real-world low-dose injection. In the prospective study, the
35 quantification accuracy was evaluated with the agreement of SUVs in the liver, the blood pool,
36 and the muscle between the DPR and the OSEM images. Quantitative analysis was also performed
37 with the SUV and the TLR in lesions, furthermore on small lesions with a diameter no more than
38 10mm. In addition, qualitative analysis was performed using a 5-point Likert scale on the
39 following perspectives: contrast, noise, and diagnostic confidence.

40 **Results** The protocols used in the study were verified to meet the EANM EARL2 requirements. In
41 the retrospective study, the DPR group with one-third acquisition time can yield a comparable

1 image quality to the reference. In the prospective study, good agreement of the SUVs between
2 DPR and OSEM was found in all the selected background tissues even if the injected dose was
3 reduced to 1/3. Both quantitative and qualitative results demonstrated that the DPR_1/3 group
4 showed no significant difference with the reference regarding the liver COV and subjective scores.
5 The lesion SUVs and TLRs in the DPR_1/3 group were significantly enhanced compared with the
6 reference, even for small lesions.

7 **Conclusions** The proposed DPR method can reduce the injected dose of SAFOV-PET scan by up
8 to 2/3 in a real-world deployment while maintaining image quality.

9
10 **Keywords** PET; deep progressive learning; low dose; image quality
11

12

1 **Declarations**

2

3 **Funding**

4 This study is supported by National Natural Science Foundation of China (81971647), Shanghai
5 Shenkang Hospital Development Center Clinical Study Project (SHDC2020CR2057B).

6

7 **Conflicts of interest/Competing interests**

8 Ying Wang, Jingyi Wang, Yang Lv, Yun Dong and Zheng Qian are all full-time employees of
9 United Imaging Healthcare, China. All other authors have no conflicts of interest to report.

10 **Availability of data and material**

11 Data are available on request to the corresponding author.

12 **Code availability**

13 Not applicable.

14 **Authors' contributions**

15 Study conception and design: Yan Xing and Jinhua Zhao

16 Material preparation and data collection: Jingyi Wang and Yun Dong

17 Data analysis: Wenli Qiao, Yang Lv and Zheng Qian

18 Drafting of the manuscript: Taisong Wang and Ying Wang

19 All authors commented on previous versions of the manuscript and read and approved the final
20 manuscript.

21 **Ethics approval**

22 All procedures performed in studies involving human participants were in accordance with the
23 ethical standards of the institutional and/or national research committee and with the 1964
24 Helsinki declaration and its later amendments or comparable ethical standards.

25 **Consent to participate**

26 The need for written informed consent in the retrospective study was waived by the Institutional
27 Review Board of Shanghai General Hospital and all participate in the prospective study signed the
28 informed consent prior to the study.

29 **Consent for publication**

30 Patients signed informed consent regarding publishing their data and photographs for scientific
31 use.

32

1 Introduction

2 Positron emission tomography (PET) is a non-invasive molecular imaging modality widely used
3 in oncology, neurology, cardiology, and other fields [1-8]. Good image quality and accurate
4 quantification of radiotracer are vital for the clinical diagnosis, prognosis, staging/restaging, and
5 treatment monitoring. However, the key confounding factors are high noise and low spatial
6 resolution of PET images [9]. The signal-to-noise ratio (SNR) of PET images for a given scanner,
7 as a metric to assess the image quality, is proportional to the square root of the product of the
8 system sensitivity, the injected activity, and the acquisition time. Reducing the injected activity or
9 the acquisition time is favored concerning the radiation exposure or patient comfort, while the
10 image quality is maintained at an acceptable level for clinical use. With the advent of the
11 state-of-the-art TB-PET scanner, the system sensitivity can be improved by a factor of 40-fold,
12 allowing for ultra-high image quality [10]. The TB-PET scanner (uEXPLORER, United Imaging
13 Healthcare, Shanghai, China) is composed of 8 PET units along the axial direction, forming the
14 system's total axial length of 194cm [11]. Due to its high cost, the availability of the TB-PET
15 scanner is limited. Thus, an approach that elevates the image quality of the standard axial
16 field-of-view (SAFOV) PET to that of the TB-PET is expected.

17
18 During the past few years, deep learning approaches have been proven to achieve superior
19 performance in denoising PET images [12-17]. It has shown the potential of low-dose to full-dose
20 conversion in various studies. During network training, the high image quality of the training pairs
21 is essential to network performance. However, direct learning from an input image to the target
22 image is challenging if the gap is large between the two images. More recently, a deep progressive
23 learning reconstruction (DPR) algorithm for PET is proposed to bridge the gap between
24 low-quality images and high-quality images through multiple learning steps [18]. The training
25 data used in the network come from the TB-PET images with an acquisition time of 900 sec,
26 which can generate an excellent image quality. Thus, we hypothesizes that the proposed DPR
27 algorithm can help the SAFOV PET/CT scanners to reconstruct PET images with comparable
28 quality to that of a TB-PET scanner.

29
30 To validate the proposed DPR algorithm, we firstly investigated the performance of the DPR
31 algorithm in shortening the acquisition time with the retrospective data. The fast acquisition is to
32 simulate the reduced injected activity in PET imaging and provide evidence for the subsequent
33 study with real-world low-dose injection. Thus, the patients were prospectively enrolled with an
34 injection of reduced activity based on the above results. The image quality of these patients was
35 comprehensively evaluated regarding quantification accuracy, lesion contrast as well as visual
36 assessment.

37
38 This study aimed to investigate the image quality of ^{18}F -FDG PET images reconstructed by the
39 DPR algorithm in patients with both a simulated and real-world low injected activity, and compare
40 to that reconstructed by the standard ordered subset expectation maximization (OSEM) algorithm.

1 Methods

2 DPR algorithm

3 The problem of PET image reconstruction is to recover an image $\mathbf{x} \in \mathbb{R}^N$ from the noisy linear
4 measurement $\mathbf{y} \in \mathbb{R}^M$ of the form

$$5 \quad \mathbf{y} = \mathbf{A}\mathbf{x} + \mathbf{r} + \mathbf{e} \quad (1)$$

6 where $\mathbf{A} \in \mathbb{R}^{M \times N}$ is the system matrix, \mathbf{r} is the random and the scatter estimate, and \mathbf{e} is the
7 additive noise. In the framework of the unrolled method for deep learning based iterative image
8 reconstruction algorithms [19], the maximum likelihood estimate of the unknown image \mathbf{x} can
9 be calculated as

$$10 \quad \hat{\mathbf{x}} = \arg \max_{\mathbf{x}} \{L(\mathbf{y} | \mathbf{x}) - \frac{\lambda}{2} \|\mathbf{x} - \mathbf{z}\|^2\} \quad (2)$$

11 where $L(\mathbf{y} | \mathbf{x})$ is the log-likelihood function, and $\mathbf{z} = \mathbf{f}(\mathbf{x}; \boldsymbol{\theta})$ is a convolutional neural network
12 (CNN) representation of an image \mathbf{z} with input image \mathbf{x} and parameters $\boldsymbol{\theta}$. The DPR
13 algorithm suggests that the network \mathbf{f} could be decomposed into many sub-networks to make
14 the network training easier. Our current implementation employs two sub-networks, that is,

$$15 \quad \mathbf{f} = \mathbf{f}_{DE} \circ \mathbf{f}_{EH}, \quad (3)$$

16 where $\mathbf{f}_{DE}: \mathbf{x} + \nu \rightarrow \mathbf{x}$ represents the denoising network (CNN-DE) which can remove the
17 noise ν from the input image, and $\mathbf{f}_{EH}: \mathbf{x}^{(k)} \rightarrow \mathbf{x}^{(k+q)}$ represents the enhancement network
18 (CNN-EH) which maps from a low convergent image $\mathbf{x}^{(k)}$ to a high convergent image $\mathbf{x}^{(k+q)}$.

19 Both CNN-DE and CNN-EH are trained based on the designed feedback network (FB-Net), as
20 shown in Fig. 1. The result of the third branch is considered to be the output of the network, which is
21 a denoised/enhanced intermediate PET image for the next iteration. The details of network design
22 and algorithm implementation could be found in our previous work [18].

24 Network training and testing

25 One hundred patient data were collected for network training and testing. The injected dose of
26 ^{18}F -Fluorodeoxyglucose (FDG) was 3.7~4.4 MBq/kg, while the acquisition time was fixed at 900 s
27 for TB-PET imaging with uEXPLORER. Benefits from its ultra-high sensitivity, uEXPLORER has
28 demonstrated its ability to provide clinically acceptable images for a scan as short as 60 s and good
29 images for a scan of more than 180 s. So a 900-s scan is long enough to generate excellent images
30 with very low image noise and high image contrast. For CNN-DE, PET images with 10% uniformly

1 down-sampled counts were used as training input, and PET images with full counts were used as
2 training targets. For CNN-EH, PET images with insufficient iterations were used as training input,
3 and PET images with sufficient iterations were used as training targets. The training image size was
4 249x249x671 with a voxel size of 2.4x2.4x2.68 mm³. The reconstruction algorithm was OP-OSEM
5 with time-of-flight (TOF) and resolution modeling. All necessary corrections like scatter,
6 normalization, dead time, attenuation, random, decay corrections were applied. Totally 53680
7 image pairs from 80 patients were used to construct the training dataset. The training data were
8 augmented via flipping and rotating, and applied with z-score normalization before they were fed
9 into the network.

10
11 The network parameters were initialized with Kaiming initialization. The loss function was the sum
12 of the L1 losses of all three branches. The training of the network took the loss function as the
13 objective function and the backpropagation algorithm was used to update the parameters based on
14 the adaptive moment estimation optimization algorithm and cyclical learning rate. The minimum
15 and maximum values for the cyclical learning rate were 1e-5 and 1e-4, respectively. The training
16 settings were the same for both CNN-DE and CNN-EH. All the training was conducted using
17 Pytorch 1.5.0 on a computer cluster of 4x NVIDIA Quadro RTX 6000 GPU. The CUDA library was
18 10.2, and cuDNN was 7.6. The trained networks were tested with 13420 image pairs from the other
19 20 patients to ensure that they could be used in this study.

21 **Algorithm evaluation**

22 The performance of the proposed DPR algorithm was evaluated through three stages of studies.
23 The phantom study verified the effectiveness of reconstruction protocols. The retrospective patient
24 study simulated the low-dose scenario using reduced scan durations, providing evidence for the
25 subsequent prospective study with real-world low-dose injection.

27 **Phantom study**

28 The phantom study used a CTN anthropological chest phantom that had two polystyrene-filled
29 chambers and a uniform background to mimic the lung and the other soft tissue in the chest. Seven
30 spherical lesions (diameter = 7, 10, 13, 17, 22, 28, and 37 mm) were placed in the phantom
31 background and five spherical lesions (diameter = 10, 10, 13, 17, 22 mm) in the polystyrene-filled
32 chambers. All spherical lesions and the phantom background were filled with 18F solution, and
33 the concentration at the 1st experiment scan start time were 23.6 and 6.2 kBq/mL, respectively,
34 resulting in a 3.81:1 lesion-to-background concentration ratio. In addition to the first experiment,
35 two delayed experiments were conducted to evaluate the image quality at the lower activity. The
36 intervals between the first and second, second, and third experiments were 110 min and 65 min,
37 respectively. Thus, the actual active concentrations at the start time of the second and third
38 experimental scans were 1/2 and 1/3 of that of the first experiment, respectively. For each
39 experiment, the CTN phantom was repeatedly scanned five times, with 2 min per scan with a
40 digital PET/CT scanner (uMI 780, United Imaging Healthcare, China).

41
42 The phantom data were reconstructed with both OSEM and DPR algorithms. The OSEM
43 algorithm was applied with two iterations, 20 subsets, a Gaussian filter with full width at half

1 maximum of 3 mm, 192×192 matrix, 600 field-of-view (FOV), 2.68 mm slice thickness, as well as
2 TOF and resolution modeling. The standard corrections (scatter, random, dead time, decay,
3 attenuation, and normalization) were included in the reconstruction. The DPR algorithm was
4 applied with the same FOV, matrix, and slice thickness as in the OSEM. No other post-processing
5 method was included in the reconstruction. The reconstructed PET images were analyzed using
6 the phantom analysis toolkit provided by SNMMI (<http://www.snmmi.org/PAT>). Recovery
7 coefficients (RC) of the spherical lesions and background coefficient of variation were recorded
8 and used as quantitative measurements to evaluate the performance of different algorithms.

10 **Patient study**

11 **Patients**

12 The study included two patient cohorts, a retrospective and a prospective one. Twenty-six and
13 forty-one oncological patients (female/male: 19/33, age: 24-87 years) referred to the Shanghai
14 General Hospital from Nov. 2020 to Sep. 2021 for clinical ¹⁸F-FDG PET/CT examinations were
15 enrolled, respectively. Their demographic and clinical information are listed in Table 1.

16 All patients had fasted for at least 6 h, and a blood glucose level was confirmed to be ≤ 10
17 mmol/mL before the ¹⁸F-FDG injection. A weight-based ¹⁸F-FDG (full and one-third) dose was
18 administered to the patient of the two cohorts using a fully automated PET infusion system
19 (MEDRAD, Bayer Medical Care Inc. Pennsylvania, USA) that allows an accurate dose
20 administration. During the uptake period of about 60 min, the patients were hydrated orally with
21 0.5-1.0 L of water.

22 This study was approved by the Institutional Review Board of Shanghai General Hospital, and the
23 written informed consent was waived in the retrospective part and obtained from the patients in
24 the prospective part.

25 **PET/CT imaging and reconstruction**

26 The same PET/CT scanner was used for image acquisition for both cohorts. Patients were firstly
27 scanned with CT with a fixed tube voltage of 120 kV and an auto-mAs technique for dose
28 modulation, providing anatomical information and attenuation correction to PET images.
29 Subsequently, patients were scanned with PET in step-and-shoot mode. PET data were acquired in
30 list-mode for 120 s and 360 s per bed position in the retrospective and prospective study.

31 The same reconstruction protocols as in the phantom study were used to reconstruct the acquired
32 PET images (hereinafter referred to as OSEM_full and DPR_full). In the retrospective study, we
33 rebinned the list-mode PET data to 60, 40, and 30 s per bed position to simulate the 1/n (n=2, 3, 4)
34 of the injected activity. The DPR algorithm was also applied to the rebinned PET data (hereinafter
35 referred to as DPR_1/2, DPR_1/3 and DPR_1/4). In the prospective study, PET images were
36 reconstructed using the first 120 s data and extended the acquisition time to 180 s and 360 s per
37 bed position to simulate the 1/2 and full dose scenarios. The DPR algorithm was also applied to
38 the acquired and rebinned PET data (hereinafter referred to as DPR_1/3, DPR_1/2 and DPR_full).

1 **Image analysis in the retrospective study**

2 In the retrospective study of this work, the image quality was quantitatively assessed on an
3 advanced workstation (uWS-MI, United Imaging Healthcare, Shanghai, China). For each patient,
4 a volume of interest (VOI) with a diameter of 30 ± 3 mm was manually drawn at the same position
5 and the slice on a homogeneous area of the right liver lobe. The SUV_{mean} and standard deviation
6 (SD) within the VOI were recorded. The liver COV, as a measure of background noise, was
7 obtained by dividing the SD by the SUV_{mean}.

8 Regarding the lesions, SUV_{max} of the identified FDG-avid lesions was measured by placing a
9 VOI to encompass the whole lesion. Thus, tumor-to-liver ratio (TLR), as a measure of image
10 contrast, was obtained by dividing the lesion SUV_{max} by the liver SUV_{mean}.

11 **Image analysis in the prospective study**

12 In the prospective study, the same nuclear medicine physician analyzed the images on the same
13 workstation as in the retrospective study. Similarly, a VOI was manually drawn at the right liver
14 lobe, aorta, and gluteus maximus. The SUV_{mean} and standard deviation (SD) of the VOI for each
15 series were recorded. The liver and the muscle COV were obtained by dividing the SUV_{mean} by
16 its SD. The value of SUV_{max} and TLR for each identified lesion was obtained using the same
17 method as the above. In addition, the diameter of the lesion was measured on the CT images.

18 Subsequently, the qualitative image quality of unlabelled images was assessed by two nuclear
19 medicine physicians (XY, 17 years' experience and WTS, 18 years' experiences) in a randomized
20 order. The patient's clinical information, as well as the acquisition duration and reconstruction
21 algorithm, were blinded to the reader. The physicians viewed both the maximum intensity
22 projection (MIP) and transverse PET images and judged the image quality using a 5-point Likert
23 scale in the following three perspectives: image contrast, image noise, and diagnostic confidence
24 (with 1=worst and 5=best). A score of 3 was given to images that were acceptable for clinical
25 diagnosis.

26 **Statistical analysis**

27 Continuous parameters are presented as the mean \pm SD and range. Fisher's exact test was
28 performed to investigate the distribution of the gender in the two cohorts. An independent *t*-test
29 was used to test the other demographic parameters of the enrolled patients from the two cohorts.
30 Bland-Altman plot analyses were performed to assess the agreement of the SUVs between the
31 reference and DPR images. All the quantitative parameters were tested for normality using the
32 Kolmogorov-Smirnov test and the two-tailed paired samples *t*-test was subsequently performed.
33 Inter-rater reliability was evaluated using Cohen's weighted kappa (linear) coefficient. The scores
34 of the qualitative image quality were subsequently compared using the Wilcoxon signed-rank test.
35 Statistical significance was considered for a p-value less than 0.05, and all statistical tests were
36 performed using SPSS Statistics, version 25 (IBM, Armonk, NY, USA) and R package.

1 **Results**

2 **Phantom study**

3 The current reconstruction protocol for both DPR and OSEM satisfies the minimum allowable RC
4 values as the EANM EARL2 requires [20]. Moreover, the SUV_{peak} difference between these two
5 algorithms is within 10%, which shows good consistency on the quantitation accuracy. As the
6 activity decreases from 6.2 kBq/ml to 2.1 kBq/ml, the background COV of DPR image increases
7 from 6.0% to 7.2% while that of OSEM image increases from 12.2% to 20.2%. DPR image has
8 much lower noise than OSEM in low-dose PET imaging (Fig. 2).

9
10 The phantom study verified the effectiveness of our current reconstruction protocols, which would
11 be used in the subsequent patient study.

12 **Retrospective patient study**

13 The liver SUV_{mean} agreed well as shown in Bland-Altman plots (Fig. 3), and no significant
14 difference was found between the DPR groups and the reference (all $p > 0.05$). The liver COV in
15 the DPR_{1/3} group showed no significant difference with that in the reference ($p = 0.955$),
16 indicating a comparable image quality (Fig. 4). The image quality of the DPR_{1/2} and DPR_{full}
17 groups was significantly improved with a reduced COV (both $p < 0.001$). Both the lesion SUV_{max}
18 and TLR in all the DPR groups showed significant enhancement compared to those in the
19 reference (all $p < 0.001$), indicating an improvement on lesion conspicuity. Based on the above
20 results, we concluded that the DPR algorithm can reduce the acquisition time to 1/3. Thus, in the
21 subsequent prospective study, the image quality of the patients injected with 1/3 of 18F-FDG was
22 analyzed.

24 **Prospective patient study**

25 In the prospective study, we analyzed the uptake of background tissues, including the liver, blood
26 pool and muscle, and found that the values of SUV_{mean} agreed well between groups as shown in
27 the Bland-Altman plots (Fig. 5). Subsequently, the COVs of the background tissues were
28 compared (Fig. 6). There was no significant difference of the COVs between the DPR_{1/3} group
29 and the reference ($p = 0.055$, 0.526 and 0.604 for the liver, blood pool and muscle, respectively),
30 while the COVs in the DPR_{1/2} and DPR_{full} group were both found significantly reduced than
31 those in the reference (both $p < 0.001$). Thus, the image quality of the DPR_{1/2} and DPR_{full}
32 groups were improved, while the DPR_{1/3} images showed a comparable quality with the
33 reference.

34
35 A total of 98 lesions were identified and included in the quantitative analysis. The SUV_{max} and
36 TLR of the lesions in all the DPR groups were significantly larger than those in the reference
37 group (all $p < 0.001$, as shown in Fig. 7). The enhancement of the lesion uptake in the DPR images
38 can be observed in the MIP and transverse images. Figure 8 illustrated PET images of a 31-year
39 old man with Hodgkin's lymphoma. Both the MIP and transverse images of the DPR images
40 showed an improved lesion detectability. Meanwhile, the DPR images demonstrated a non-inferior
41 performance in the noise level compared to the reference.

1 A further study was performed on the small lesions with a diameter of less than 10 mm (n=27). In
2 all the DPR images, a significantly higher uptake was also found than that in the OSEM images
3 (all $p < 0.001$). Likewise, the TLR in the DPR groups showed significant improvement compared
4 with that in the OSEM group (all $p < 0.001$).

5
6 In the visual analysis, the weighted kappa coefficient was 0.612, indicating a substantial
7 agreement of the subjective score between the two readers. There were no significant differences
8 between the DPR_1/3 group and the reference regarding the contrast, noise and diagnostic
9 confidence ($p = 0.284$, 0.655 and 0.137 , respectively). Both the DPR_1/2 and DPR_full groups
10 showed significantly higher scores than the reference regarding all the three perspectives (all
11 $p < 0.001$, as shown in Fig. 9).

13 Discussion

14 In this study, we investigated the image quality of a deep-progressive learning algorithm with both
15 simulated and real-world reduced injected dose. As known, PET is associated with the detection of
16 annihilation photons that are produced back-to-back after positron emission from a radioactive
17 tracer. Hence, radiation exposure is inevitable in PET imaging, and the injected dose should be
18 reduced while maintaining adequate image quality that provides sufficient clinical information.
19 Particularly for longitudinal studies when multiple PET/CT scans are performed, it is desirable to
20 adapt the injected dose to the lowest level to reduce the accumulated dose. In addition, concerns
21 on radiation exposure are of great interest in paediatric populations because the risk of
22 radiation-induced carcinogenesis is higher in children and thus prone at risk to developing
23 secondary tumors during their lifetime [21-23].

24 The advent of the total-body or long axial field-of-view (LAFOV) PET scanners has made a
25 breakthrough on the system sensitivity which can be greatly beneficial to reduce the injected dose.
26 Previous studies have been performed with half and even 1/10 of the dose on both oncological
27 patients and healthy volunteers, and demonstrated the feasibility of low-dose and ultra-low-dose
28 using the TB PET scanner [24-28]. However, up to now, there are only a limited number of TB or
29 LAFOV PET/CT scanners available worldwide. For the rest of the PET sites, an alternative
30 solution by applying the deep learning technology is more reasonable for the low-dose PET scans.
31 Several studies have shown the promising performance of CNN-based methods in improving the
32 PET image quality with reduced acquisition time or the injected activity while maintaining
33 adequate information for diagnosis and quantification accuracy. In this work, the phantom study
34 was performed to verify the harmonization of the selected reconstruction protocols as the EANM
35 EARL2 requires. Subsequently, both the simulated and real-world low-dose DPR images were
36 evaluated and compared with the standard OSEM images and showed that the image quality can
37 be maintained even the injected dose was reduced to 1/3. In addition, this work comprehensively
38 evaluated the image quality by using quantitative parameters and subjective scores.

39 During the network training, high-quality images reconstructed from high injected dose or long
40 acquisition time are required to be used as the training labels. High injected dose in PET imaging
41 is related to the potential safety concerns and is not employed in clinical practice. On the other
42 hand, a longer acquisition time may adversely degrade the image quality due to the patient's
43 motion during the acquisition. An alternative solution is to adapt the regularised images with less

1 noise and better contrast, such as block sequential regularised expectation maximization (BSREM)
2 [17, 29-32]. Moreover, the employment of the TB-PET images can make an unprecedented
3 breakthrough on the image quality of the training dataset. The proposed DPR method utilized two
4 learning steps to transfer the low-quality images to high-quality images and is feasible for both
5 reducing noise and improving image contrast. A shortcoming of the CNN-based methods is that
6 the performance is usually degraded on small lesions since they are overwhelmed by the image
7 noise in low SNR images. The proposed DPR method can tackle this problem by incorporating the
8 networks into the iteration process [18]. In a previous study on the same network, even the
9 smallest hot sphere with a diameter of 10 mm in an IEC body phantom still showed at least 2 folds
10 contrast to noise (CNR) gain. Consistent results were found with the clinical data in this study.
11 The DPR algorithm on the small lesions still showed good performance regarding both the
12 quantitative SUV measurements and TLR values.

13 The present study has several limitations. First, the work was a single-centre study with a limited
14 number of enrolled patients. A large-scale multi-centre study is expected to be performed,
15 especially on the quantification accuracy of SUVs. In addition, the difference of physiological
16 uptake was observed between the images reconstructed by the first two-minute data and the last
17 two-minute data in the prospective study. Currently, we rebinned the first two-minute data to
18 reconstruct DPR images for analysis. Furthermore, the supervised network in the work was trained
19 with ^{18}F -FDG PET data and this study only enrolled oncological patients who underwent ^{18}F -FDG
20 PET examinations. In future work, the performance of the DPR algorithm can be evaluated with
21 other non- ^{18}F -FDG tracers, such as ^{68}Ga -PSMA.

22 **Conclusion**

23 In this work, a total-body PET guided deep progressive learning method was proposed for
24 reducing the noise and improving the contrast of ^{18}F -FDG low-dose PET images. Both the
25 simulated and real-world low-dose studies demonstrated that PET imaging with the DPR
26 algorithm can reduce the injected dose to 1/3 of the standard without compromising the image
27 quality and small lesion detectability. This study has shown the potential of the proposed DPR
28 algorithm in low-dose PET imaging for conventional digital PET/CT scanners in clinical routines.
29

1 Reference

- 2 1. Boellaard R, et al. FDG PET/CT: EANM procedure guidelines for tumour imaging: version
3 2.0. *Eur J Nucl Med Mol Imaging*. 2015;42(2):328–54
- 4 2. Anand SS, Singh H, Dash AK. Clinical Applications of PET and PET-CT. *Med J Armed*
5 *Forces India*. 2009;65(4):353-358. doi:10.1016/S0377-1237(09)80099-3
- 6 3. Fletcher JW, Djulbegovic B, Soares HP, Siegel BA, Lowe VJ, Lyman GH, et al.
7 Recommendations on the use of 18F-FDG PET in oncology. *J Nucl Med*. 2008;49:480–508.
8 <https://doi.org/10.2967/jnumed.107.047787>.
- 9 4. Beyer T, Townsend DW, Brun T, Kinahan PE, Charron M, Roddy R, et al. A combined
10 PET/CT scanner for clinical oncology. *J Nucl Med*. 2000;41:1369–79.
- 11 5. Dilsizian V, Bacharach SL, Beanlands RS, et al. ASNC imaging guidelines/SNMMI procedure
12 standard for positron emission tomography (PET) nuclear cardiology procedures. *J*
13 *NuclCardiol*. 2016;23(5):1187-1226. doi:10.1007/s12350-016-0522-3
- 14 6. Schwaiger M, Ziegler S, Nekolla SG. PET/CT: challenge for nuclear cardiology. *J Nucl Med*.
15 2005;46:1664–78.
- 16 7. deKemp RA, Yoshinaga K, Beanlands RS. Will 3-dimensional PET-CT enable the routine
17 quantification of myocardial blood flow?. *J NuclCardiol*. 2007;14(3):380-397.
18 doi:10.1016/j.nuclcard.2007.04.006
- 19 8. Tai YF. Applications of positron emission tomography (PET) in neurology. *J NeurolNeurosurg*
20 *Psychiatry*. 2004;75:669–76. <https://doi.org/10.1136/jnnp.2003.028175>.
- 21 9. Liu J, Malekzadeh M, Mirian N, Song TA, Liu C, Dutta J. Artificial Intelligence-Based Image
22 Enhancement in PET Imaging: Noise Reduction and Resolution Enhancement. *PET Clin*.
23 2021;16(4):553-576. doi:10.1016/j.cpet.2021.06.005
- 24 10. Cherry SR, Jones T, Karp JS, Qi J, Moses WW, Badawi RD. Total-Body PET: Maximizing
25 Sensitivity to Create New Opportunities for Clinical Research and Patient Care. *J Nucl Med*.
26 2018;59(1):3-12. doi:10.2967/jnumed.116.184028
- 27 11. Spencer BA, Berg E, Schmall JP, et al. Performance Evaluation of the uEXPLORER
28 Total-Body PET/CT Scanner Based on NEMA NU 2-2018 with Additional Tests to
29 Characterize PET Scanners with a Long Axial Field of View. *J Nucl Med*. 2021;62(6):861-870.
30 doi:10.2967/jnumed.120.250597
- 31 12. Sanaat A, Shiri I, Arabi H, Mainta I, Nkoulou R, Zaidi H. Deep learning-assisted
32 ultra-fast/low-dose whole-body PET/CT imaging [published online ahead of print, 2021 Jan
33 25]. *Eur J Nucl Med Mol Imaging*. 2021;10.1007/s00259-020-05167-1.
34 doi:10.1007/s00259-020-05167-1
- 35 13. Cui J, Gong K, Guo N, et al. PET image denoising using unsupervised deep learning. *Eur J*
36 *Nucl Med Mol Imaging*. 2019;46(13):2780-2789. doi:10.1007/s00259-019-04468-4
- 37 14. Sanaat A, Arabi H, Mainta I, Garibotto V, Zaidi H. Projection Space Implementation of Deep
38 Learning-Guided Low-Dose Brain PET Imaging Improves Performance over Implementation
39 in Image Space. *J Nucl Med*. 2020;61(9):1388-1396. doi:10.2967/jnumed.119.239327
- 40 15. Schaefferkoetter J, Yan J, Ortega C, et al. Convolutional neural networks for improving image
41 quality with noisy PET data. *EJNMMI Res*. 2020;10(1):105. Published 2020 Sep 21.
42 doi:10.1186/s13550-020-00695-1
- 43 16. Wang YJ, Baratto L, Hawk KE, et al. Artificial intelligence enables whole-body positron

- 1 emission tomography scans with minimal radiation exposure [published online ahead of print,
2 2021 Feb 1]. *Eur J Nucl Med Mol Imaging*. 2021;10.1007/s00259-021-05197-3.
3 doi:10.1007/s00259-021-05197-3
- 4 17. Mehranian A, Wollenweber SD, Walker MD, et al. Image enhancement of whole-body
5 oncology [18F]-FDG PET scans using deep neural networks to reduce noise [published online
6 ahead of print, 2021 Jul 28]. *Eur J Nucl Med Mol Imaging*.
7 2021;10.1007/s00259-021-05478-x. doi:10.1007/s00259-021-05478-x
- 8 18. Lv Y, Xi C. PET image reconstruction with deep progressive learning. *Phys Med Biol*.
9 2021;66(10):10.1088/1361-6560/abfb17. Published 2021 May 14.
10 doi:10.1088/1361-6560/abfb17
- 11 19. A. J. Reader, G. Corda, A. Mehranian, C. D. Costa-Luis, S. Ellis, and J. A. Schnabel, "Deep
12 Learning for PET Image Reconstruction," *IEEE Transactions on Radiation and Plasma*
13 *Medical sciences*, vol. PP, no. 99, pp. 1-1, 2020.
- 14 20. Kaalep A, Sera T, Rijnsdorp S, et al. Feasibility of state of the art PET/CT systems
15 performance harmonisation. *Eur J Nucl Med Mol Imaging*. 2018;45(8):1344-1361.
16 doi:10.1007/s00259-018-3977-4
- 17 21. Kleinerman RA. Cancer risks following diagnostic and therapeutic radiation exposure in
18 children. *PediatrRadiol*. 2006;36Suppl 2(Suppl 2):121-125. doi:10.1007/s00247-006-0191-5
- 19 22. Voss SD, Reaman GH, Kaste SC, Slovis TL. The ALARA concept in pediatric oncology.
20 *PediatrRadiol*. 2009;39(11):1142-1146. doi:10.1007/s00247-009-1404-5
- 21 23. Hall EJ, Brenner DJ. Cancer risks from diagnostic radiology. *Br J Radiol*.
22 2008;81(965):362-378. doi:10.1259/bjr/01948454
- 23 24. Tan H, Sui X, Yin H, et al. Total-body PET/CT using half-dose FDG and compared with
24 conventional PET/CT using full-dose FDG in lung cancer. *Eur J Nucl Med Mol Imaging*.
25 2021;48(6):1966-1975. doi:10.1007/s00259-020-05091-4
- 26 25. Zhao YM, Li YH, Chen T, et al. Image quality and lesion detectability in low-dose pediatric
27 18F-FDG scans using total-body PET/CT. *Eur J Nucl Med Mol Imaging*.
28 2021;48(11):3378-3385. doi:10.1007/s00259-021-05304-4
- 29 26. Xiao J, Yu H, Sui X, et al. Can the BMI-based dose regimen be used to reduce injection
30 activity and to obtain a constant image quality in oncological patients by 18F-FDG total-body
31 PET/CT imaging? [published online ahead of print, 2021 Jun 29]. *Eur J Nucl Med Mol*
32 *Imaging*. 2021;10.1007/s00259-021-05462-5. doi:10.1007/s00259-021-05462-5
- 33 27. Tan H, Cai D, Sui X, et al. Investigating ultra-low-dose total-body [18F]-FDG PET/CT in
34 colorectal cancer: initial experience [published online ahead of print, 2021 Aug 30]. *Eur J*
35 *Nucl Med Mol Imaging*. 2021;10.1007/s00259-021-05537-3.
36 doi:10.1007/s00259-021-05537-3
- 37 28. Hu Y, Liu G, Yu H, et al. Feasibility of ultra-low 18F-FDG activity acquisitions using
38 total-body PET/CT [published online ahead of print, 2021 Sep 30]. *J Nucl Med*.
39 2021;jnumed.121.262038. doi:10.2967/jnumed.121.262038
- 40 29. Lindström E, Sundin A, Trampal C, et al. Evaluation of Penalized-Likelihood Estimation
41 Reconstruction on a Digital Time-of-Flight PET/CT Scanner for 18F-FDG Whole-Body
42 Examinations. *J Nucl Med*. 2018;59(7):1152-1158. doi:10.2967/jnumed.117.200790
- 43 30. Baratto L, Duan H, Ferri V, Khalighi M, Jagaru A. The Effect of Various β Values on Image
44 Quality and Semiquantitative Measurements in 68Ga-RM2 and 68Ga-PSMA-11 PET/MRI

1 Images Reconstructed With a Block Sequential Regularized Expectation Maximization
2 Algorithm. *ClinNucl Med.* 2020;45(7):506-513. doi:10.1097/RLU.0000000000003075
3 31. Zanoni L, Argalia G, Fortunati E, et al. Can Q.Clear reconstruction be used to improve [68
4 Ga]Ga-DOTANOC PET/CT image quality in overweight NEN patients? [published online
5 ahead of print, 2021 Oct 25]. *Eur J Nucl Med Mol Imaging.*
6 2021;10.1007/s00259-021-05592-w. doi:10.1007/s00259-021-05592-w
7 32. Yang FJ, Ai SY, Wu R, et al. Impact of total variation regularized expectation maximization
8 reconstruction on the image quality of 68Ga-PSMA PET: a phantom and patient study. *Br J*
9 *Radiol.* 2021;94(1120):20201356. doi:10.1259/bjr.20201356

10

11

12

13

1 **Tables**

2

3 **Table 1** Patient demographic characteristics

Parameter	Retrospective study	Prospective study	P value
No. of patients	26	41	N.A.
Age (years)	63.7±16.4 [24, 87] ^a	52.9±12.2 [15, 69] ^a	0.003
Gender			
Female	8	18	0.315
Male	18	23	
Weight (kg)	65.2±12.2 [51.2, 110] ^a	61.9±12.6 [44, 101.4] ^a	0.233
Height (cm)	166.2±8.6 [150, 184] ^a	163.4±9.6 [146, 183] ^a	0.289
BMI	23.5±3.1 [17.3, 32.5] ^a	23.0±3.4 [16.3, 31.7] ^a	0.570
Glucose level	5.38±0.88 [4.3, 7.9] ^a	5.34±0.84 [3.8, 8.1] ^a	0.846
Injected activity (MBq)	258±46 [200, 407] ^a	81±15 [51, 115] ^a	<0.001
Injected activity/weight(MBq/kg)	3.97 ± 0.28[3.61, 4.75] ^a	1.32 ± 0.18[1.10, 2.11] ^a	<0.001
Uptake time (min)	70±14 [49, 97] ^a	68±16 [39, 105] ^a	0.458
Primary cancer type			N.A.
Leukaemia	1 ^b	3 ^b	
Bladder cancer	1 ^b	0	
Multiple myeloma	1 ^b	0	
Lung cancer	6 ^b	9 ^b	
Liver cancer	0	1 ^b	
Laryngeal carcinoma	1 ^b	0	
Bone tumor	1 ^b	0	
Colorectal cancer	3 ^b	2 ^b	
Lymphoma	5 ^b	8 ^b	
Ovarian cancer	1 ^b	0	
Breast cancer	1 ^b	2 ^b	
Renal cancer	1 ^b	1 ^b	
Esophageal cancer	2 ^b	2 ^b	
Gastric cancer	1 ^b	0	
Pancreatic cancer	1 ^b	1 ^b	
Pelvic carcinoma	0	1 ^b	
Tongue cancer	0	2 ^b	
Uterine cancer	0	5 ^b	
Aplastic anemia	0	1 ^b	
Popliteal fossa tumor	0	1 ^b	
Tonsil tumor	0	1 ^b	
Nasopharyngeal cancer	0	3 ^b	

4 ^aData are presented as the mean± standard deviation [minimum, maximum].

- 1 ^bNumber of patients.
- 2 N.A., not applicable; BMI, body mass index.
- 3

1 **Figure legends**

2 **Fig. 1(a)** A general scheme of the DPR algorithm. The reconstruction workflow consists of multiple
3 CNN blocks. Each block receives the output image of the previous block as the initial image for the
4 EM iterations and passes the output image to the next CNN block. (b) The network architecture of the
5 FB-Net. In this design, the network has three branches. H1, H2 and H3 are the outputs of these three
6 branches respectively. Green lines indicate residual connections between the input and the output of
7 each branch. Gray lines indicate dense connections between different layers in the FB-Block.

8
9 **Fig. 2** (a-c) are plots of recovery coefficient of spherical lesions in the 1st, 2nd and 3rd experiment,
10 respectively. (d) Bar plot of the background COV in the phantom study.

11
12 **Fig.3** Bland-Altman plots of liver SUV_{mean} between the DPR group and the reference group in the
13 retrospective study. All the DPR groups showed a good agreement on the quantification accuracy of the
14 liver SUV_{mean} with the reference.

15
16 **Fig.4** Comparison of the liver COV, lesion SUV_{max} and TLR between DPR groups and the reference in
17 the retrospective study. The liver COV showed no significant difference between the DPR_{1/3} group
18 and the reference. All the DPR groups show a significantly elevated SUV_{max} and TLR compared to
19 the reference group, indicating an improved image contrast. *** p<0.001; ns, no significant difference.
20 COV, coefficient of variance. SUV, standardized uptake value. TLR, target-to-liver ratio.

21
22
23 **Fig.5** Bland-Altman plots of the liver, the blood pool and the muscle SUV_{mean} between DPR groups
24 (from left to right: DPR_{full}, DPR_{1/2} and DPR_{1/3}) and the reference in the prospective study. SUV,
25 standardized uptake value

26
27 **Fig.6** Comparison of the liver, the blood pool and the muscle COV between DPR groups and the
28 reference. The liver, the blood pool and the muscle COV showed no significant difference between the
29 DPR_{1/3} group and the reference. All the other DPR groups show a significantly reduced COV
30 compared to the reference group, indicating an improved image quality. *** p<0.001; ns, no significant
31 difference. COV, coefficient of variance.

32
33 **Fig.7** Comparison of the lesion SUV_{max} and TLR between DPR groups and the reference (blue line: an
34 increase; orange line: a decrease). The SUV_{max} and TLR of all the DPR groups were significantly
35 improved compared to the reference group. *** p<0.001. SUV, standardized uptake value. TLR,
36 target-to-liver ratio.

37
38 **Fig.8** PET images of a 31-year old male patient diagnosed with Hodgkin's lymphoma. After injection of
39 85 MBq 18F-FDG, the patient underwent a PET scan with 6 min per bed position 77 min post-injection.
40 Both the MIP (upper row) and transverse images (middle row) demonstrated an improved lesion
41 detectability of the DPR images compared to the OSEM images. It can be observed that the image
42 noise in the liver (bottom row)

1 **Fig.9** Visual assessment of the image contrast, noise and diagnostic confidence between DPR groups
2 and the reference. All DPR groups show a significantly higher score compared to the reference group.
3 *** p<0.001.

Figures

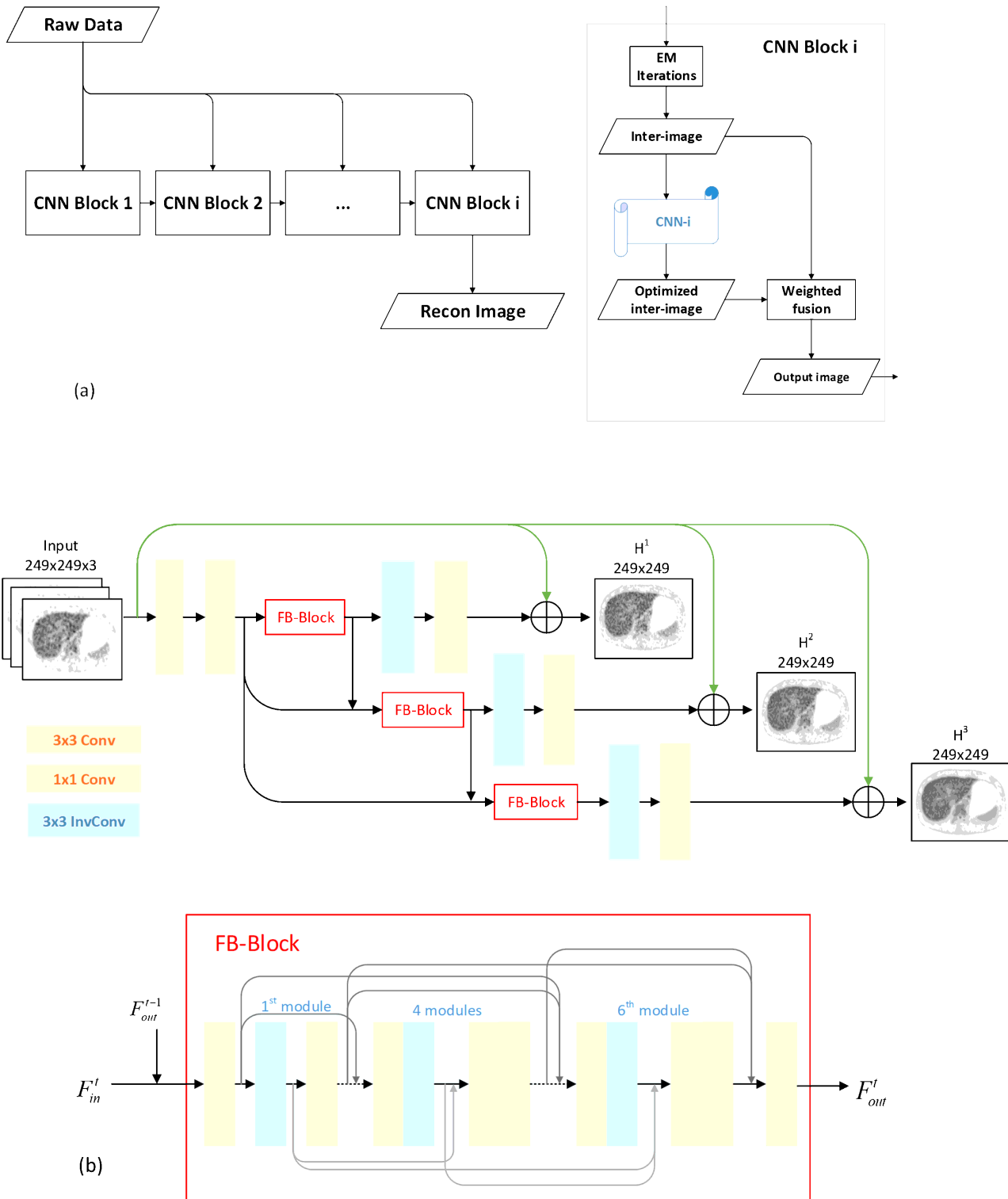


Figure 1

(a) A general scheme of the DPR algorithm. The reconstruction workflow consists of multiple CNN blocks. Each block receives the output image of the previous block as the initial image for the EM iterations and passes the output image to the next CNN block. (b) The network architecture of the FB-Net. In this design,

the network has three branches. H1, H2 and H3 are the outputs of these three branches respectively. Green lines indicate residual connections between the input and the output of each branch. Gray lines indicate dense connections between different layers in the FB-Block.

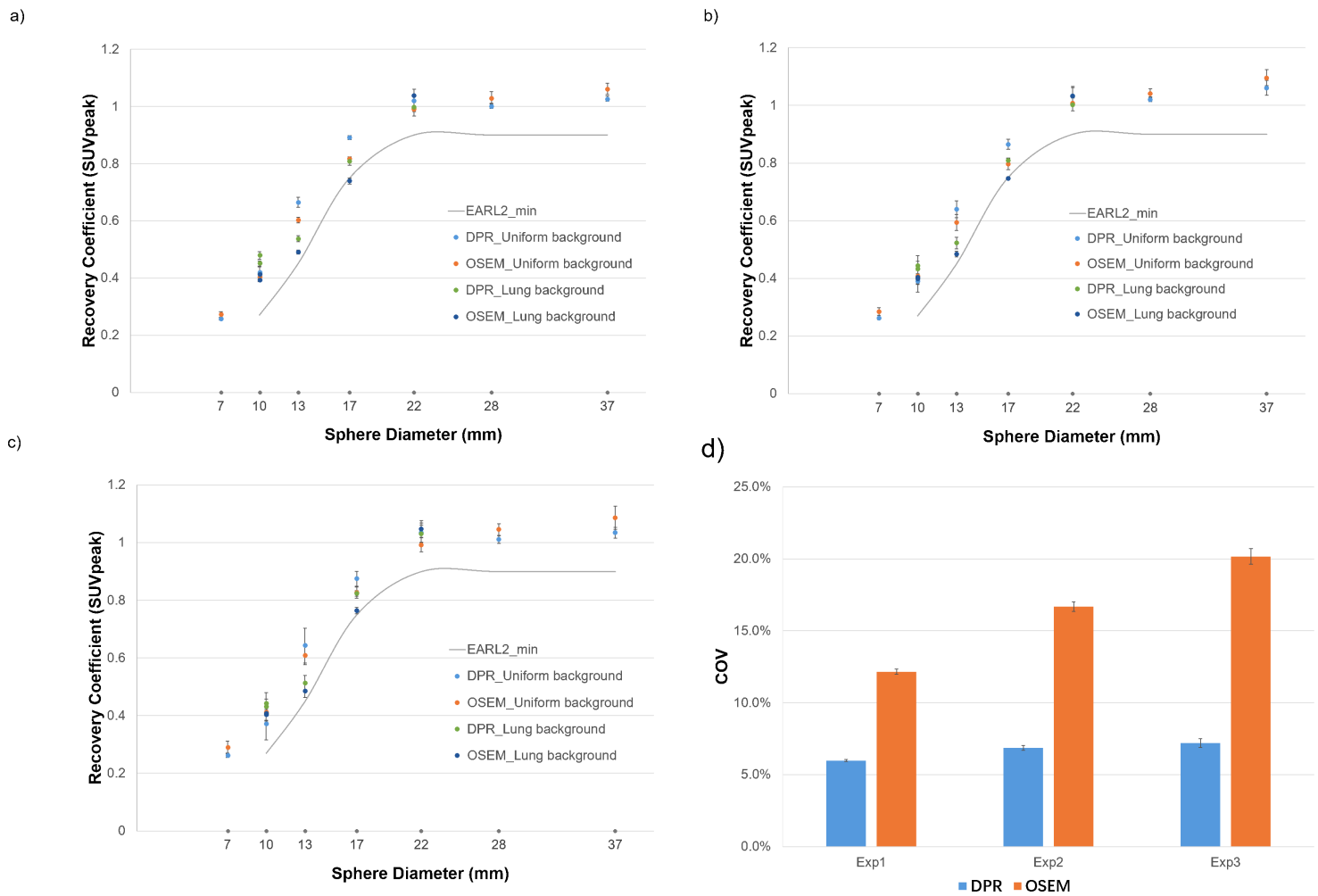


Figure 2

(a-c) are plots of recovery coefficient of spherical lesions in the 1st, 2nd and 3rd experiment, respectively. (d) Bar plot of the background COV in the phantom study.

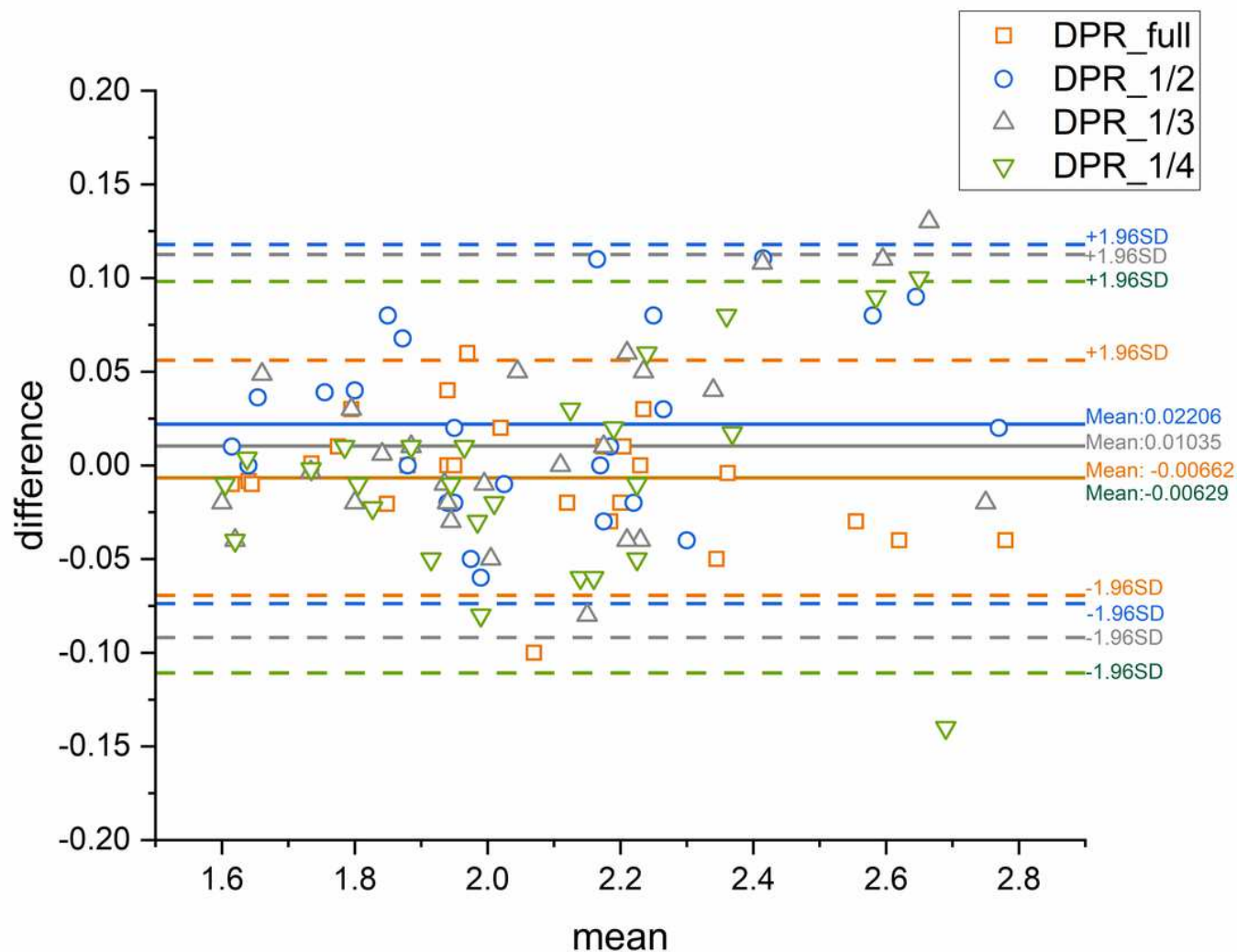


Figure 3

Bland-Altman plots of liver SUVmean between the DPR group and the reference group in the retrospective study. All the DPR groups showed a good agreement on the quantification accuracy of the liver SUVmean with the reference.

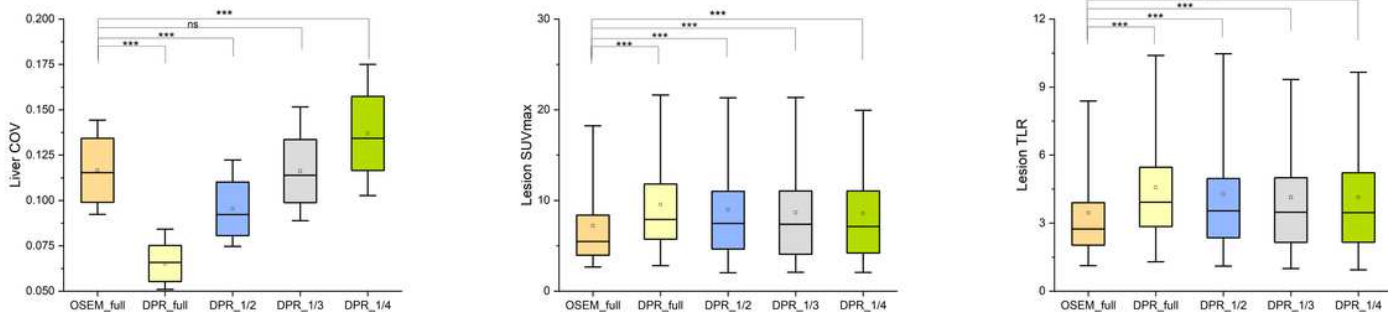


Figure 4

Comparison of the liver COV, lesion SUVmax and TLR between DPR groups and the reference in the retrospective study. The liver COV showed no significant difference between the DPR_1/3 group and the reference. All the DPR groups show a significantly elevated SUVmax and TLR compared to the reference group, indicating an improved image contrast. *** $p < 0.001$; ns, no significant difference. COV, coefficient of variance. SUV, standardized uptake value. TLR, target-to-liver ratio.

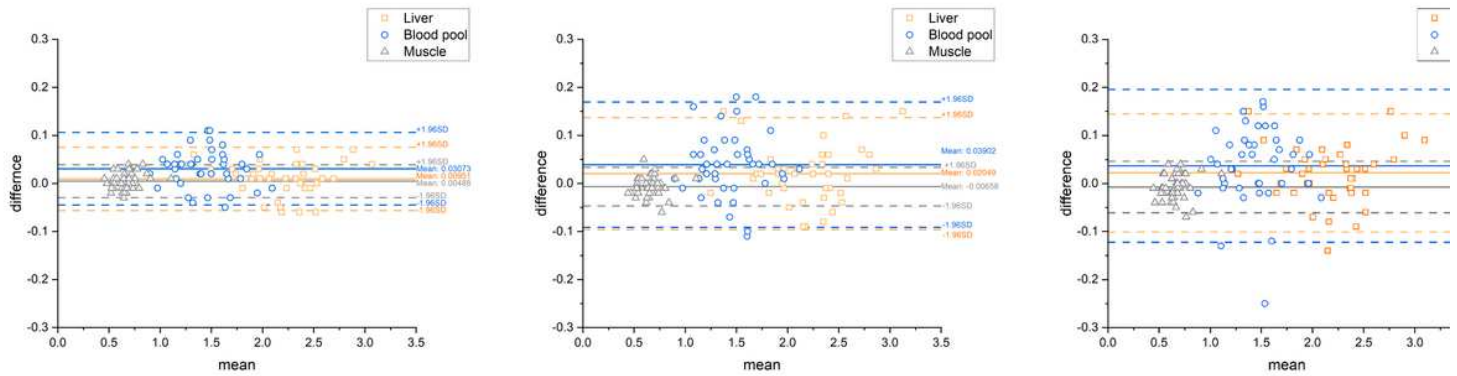


Figure 5

Bland-Altman plots of the liver, the blood pool and the muscle SUVmean between DPR groups (from left to right: DPR_full, DPR_1/2 and DPR_1/3) and the reference in the prospective study. SUV, standardized uptake value

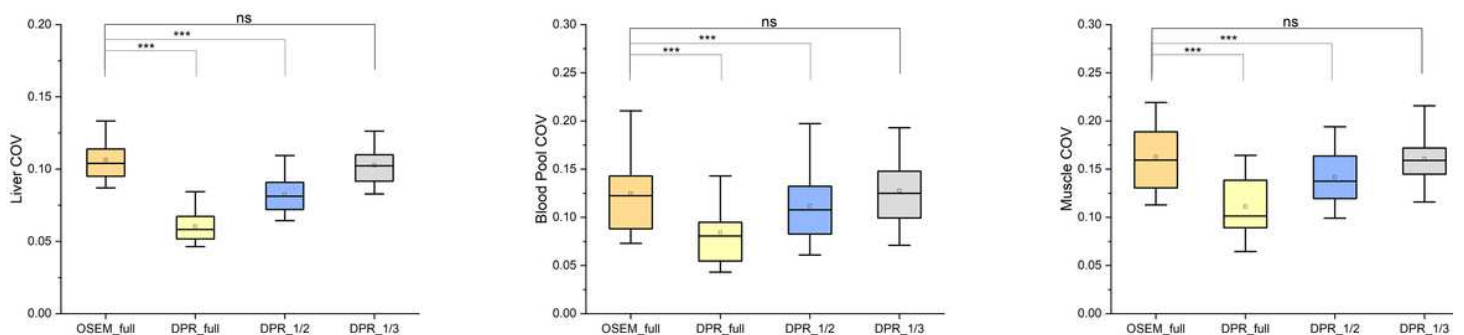


Figure 6

Comparison of the liver, the blood pool and the muscle COV between DPR groups and the reference. The liver, the blood pool and the muscle COV showed no significant difference between the DPR_1/3 group and the reference. All the other DPR groups show a significantly reduced COV compared to the reference group, indicating an improved image quality. *** $p < 0.001$; ns, no significant difference. COV, coefficient of variance.

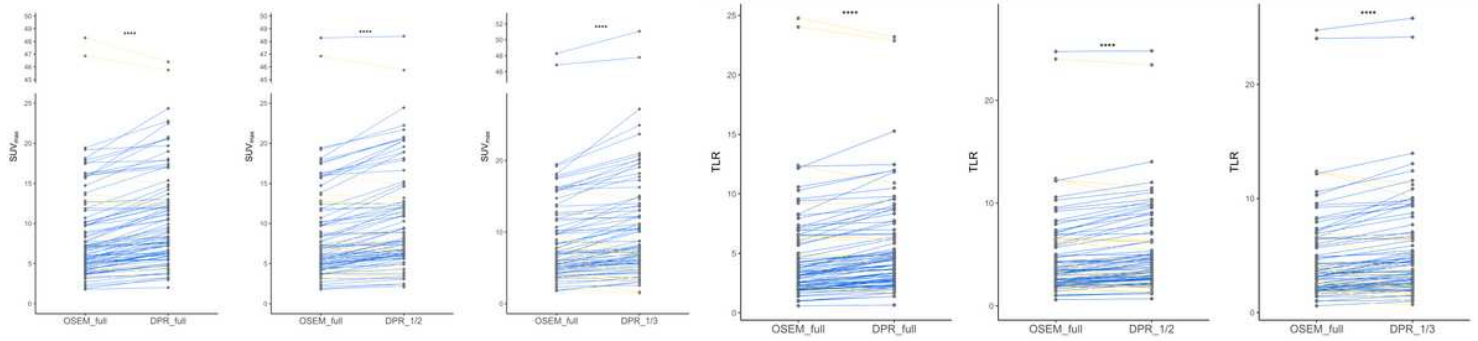


Figure 7

Comparison of the lesion SUVmax and TLR between DPR groups and the reference (blue line: an increase; orange line: a decrease). The SUVmax and TLR of all the DPR groups were significantly improved compared to the reference group. *** $p < 0.001$. SUV, standardized uptake value. TLR, target-to-liver ratio.

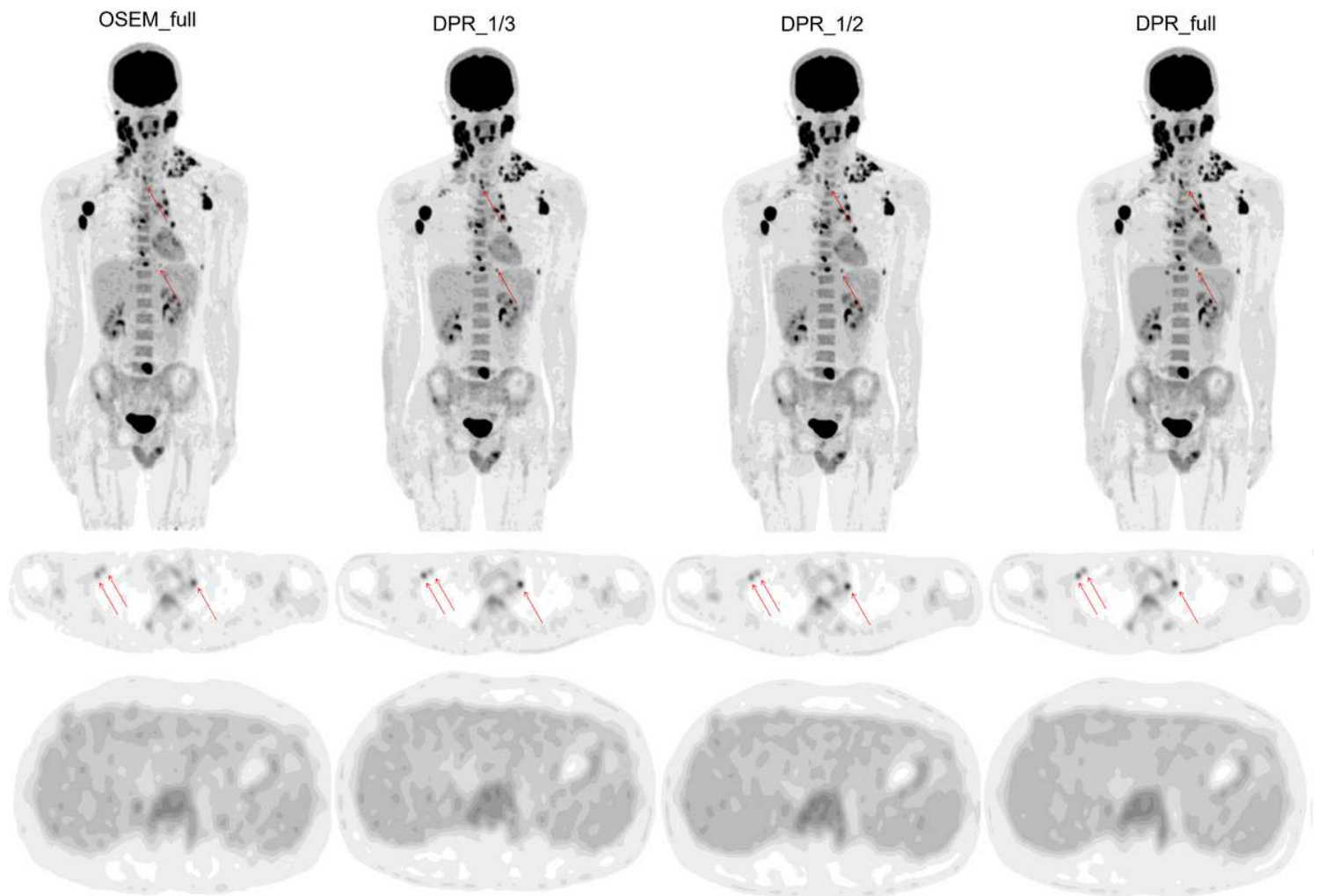


Figure 8

PET images of a 31-year old male patient diagnosed with Hodgkin's lymphoma. After injection of 85 MBq ^{18}F -FDG, the patient underwent a PET scan with 6 min per bed position 77 min post-injection. Both the

MIP (upper row) and transverse images (middle row) demonstrated an improved lesion detectability of the DPR images compared to the OSEM images. It can be observed that the image noise in the liver (bottom row)

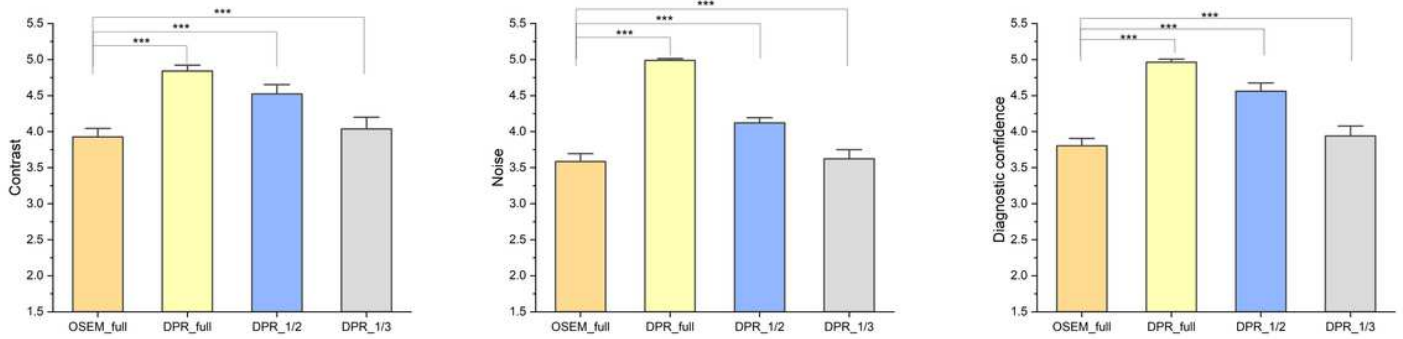


Figure 9

Visual assessment of the image contrast, noise and diagnostic confidence between DPR groups and the reference. All DPR groups show a significantly higher score compared to the reference group. *** $p < 0.001$.